# West Antarctic ice loss influenced by anthropogenic forcing and internal climate variability

Paul R. Holland[1*], Thomas J. Bracegirdle[1], Pierre Dutrieux[2], Adrian Jenkins[1], and Eric J. Steig[3]
[1]British Antarctic Survey, Cambridge, UK
[2]Lamont-Doherty Earth Observatory of Columbia University, Palisades, NY, USA
[3]Department of Earth and Space Sciences, University of Washington, Seattle, WA, USA
[*]corresponding author

**Recent ice loss from the West Antarctic Ice Sheet has been caused by ocean melting of ice shelves in the Amundsen Sea. Eastward wind anomalies at the shelf break enhance the import of warm Circumpolar Deep Water onto the Amundsen Sea continental shelf, which creates transient melting anomalies with an approximately decadal period. No anthropogenic influence on this process has been established. Here, we combine observations and climate model simulations to suggest that increased greenhouse-gas forcing caused shelf-break winds to transition from mean easterlies in the 1920s to the near-zero mean zonal winds of the present day. Strong internal climate variability, primarily linked to the tropical Pacific, is superimposed upon this forced trend. We infer that the Amundsen Sea experienced decadal ocean variability throughout the 20$^{th}$ century, with warm anomalies gradually becoming more prevalent, offering a credible explanation for the ongoing ice loss. Existing climate model projections show that strong future greenhouse-gas forcing creates persistent mean westerly shelf-break winds by 2100, suggesting a further enhancement of warm ocean anomalies. These wind changes are weaker under a scenario in which greenhouse gases are stabilised.**

The West Antarctic Ice Sheet (WAIS) has been losing ice throughout the satellite record, currently at a rate equivalent to global sea-level rise of ~4.5 cm/century (2012-2017 average)[1]. This ice loss is known to be driven by changes in ocean melting of ice shelves[2], but it remains unclear whether these changes can be attributed to contemporary climate change. The rate of ice loss shows large variations[3,4] driven by decadal variability in oceanic conditions[5,6]. However, this ocean variability does not necessarily explain the overall ice loss, since on longer timescales the WAIS could be in balance with decadally-varying forcing[7]. There is evidence that historical ocean melting anomalies caused ice streams to unground from stabilising seabed features, triggering geometrical ice and ocean feedbacks that remain active[6,8-12]. In this study, we consider the possibility that the decadal variability is superimposed on a longer-term trend, increasing the mean melt rates about which decadal variations occur.

Warm Circumpolar Deep Water (CDW) has occupied the Amundsen Sea continental shelf since the earliest observations[13] but the thickness of the CDW layer varies markedly, driving the decadal variability in melting[6,14]. Observational and modelling evidence shows that the transport of CDW onto the Amundsen Sea shelf is strongly affected by ocean surface stresses at the shelf break[5,6,14-18]. By modifying the barotropic ocean flow, eastward stress anomalies enhance an undercurrent that transports CDW on-shelf via seabed troughs, thickening the CDW layer and increasing melting[5,18,19]. Additional processes such as local sea-ice growth and wind forcing modify ocean conditions over the shelf[20-22]. However, these surface processes have less influence at greater depths, which dominate variability in ice-shelf melting, and on longer timescales, which are of greatest importance to the ice-sheet response[7]. Furthermore, local surface processes can only reduce or re-distribute the ocean heat on the shelf; CDW

import is the only process that can increase the overall on-shelf heat content. As a result, the observed history of ice-shelf melting shows a close correspondence to the import of CDW onto the shelf, which is regulated by zonal surface stresses over the shelf break[5,6]. This study relies on this established linkage between winds and ice-shelf melting and examines the wider drivers of wind anomalies, including tropical Pacific linkages, 20$^{th}$-century variability, the role of anthropogenic forcing, and future projections.

**Tropical Pacific forcing of Amundsen Sea variability**

We estimate the total ocean surface stress on the Amundsen Sea, accounting for the effect of sea ice, by combining wind data from the ERA-Interim reanalysis with satellite-tracked sea ice drift observations (Methods; ref. [23]). The Amundsen Sea shelf break sits near the centre of the Amundsen Sea Low[24], where the long-term mean zonal stress is negligible (Figure 1a). Interannual stress variability is large (Figure 1b), and its uniformity across the region implies that shelf-break stresses experience exceptionally high variability relative to their low mean. This may explain why strong ocean (and ice sheet) variability occurs in the Amundsen Sea.

Total stress and wind-only stress differ substantially over the shelf, but are highly correlated at the shelf break (Supplementary Figure S1). Therefore, throughout this study we use zonal winds over the Pine Island/Thwaites Troughs (PITT; Figure 1a) as a proxy for zonal stress and hence CDW transport onto the shelf. PITT winds contain anomalies with an approximately decadal period (Figure 2a), which dominate the variability in ice-sheet forcing[5,6]. To focus upon this variability, we hereafter apply a 2-year running mean to all quantities, isolating decadal anomalies while preserving their extrema (Supplementary Figure S2).

Maps of correlation between PITT winds and global sea-surface temperature (SST) and sea-level pressure (SLP) are shown in Figure 2b and Supplementary Figure S3. Eastward wind anomalies are associated with weakening of the Amundsen Sea Low, part of a global response to anomalies in the tropical Pacific that is transmitted by standing atmospheric Rossby waves[9,25]. The global wind anomalies induce accompanying global SST anomalies by altering Ekman transport and surface fluxes[26]. Figure 2 also shows the Southern Oscillation Index (SOI), which represents the El Niño—Southern Oscillation, and the Interdecadal Pacific Oscillation (IPO) tripole index, which represents decadal Pacific variability (Methods). PITT winds are highly correlated with these indices, which represent natural variability that is internally generated within the climate system. Indeed, PITT wind anomalies are highly correlated to all measures of tropical Pacific variability[9,14], and bear no relation to other climate indices (Supplementary Figure S4).

The strong statistical link between PITT winds and tropical Pacific SSTs provides an opportunity to constrain historical wind forcing of the Amundsen Sea, because tropical Pacific SSTs have been adequately observed since the 1920s (ref. [26]). To utilise these observations, we use an ensemble of 'pacemaker' climate model simulations[27] (PACE) to estimate PITT winds during the 20$^{th}$ century (Methods). PACE comprises 20 simulations of the Community Earth System Model (CESM) under natural and anthropogenic radiative forcings, but also constrained to follow observed tropical Pacific SST anomalies since 1920. This constraint ensures that the model winds follow the real history of the internal climate variability that is associated with the tropical Pacific. Since Pacific variability has such a strong influence on the Amundsen Sea, these simulations provide a constrained estimate of historical variability in PITT winds.

Each simulation within the PACE ensemble represents a single realisation of the climate, so the real winds can be considered as being comparable to an individual ensemble member. The mean and variability of PITT winds in the PACE simulations compare very favourably with ERA-Interim (Figure 3a). The PACE ensemble mean represents the mean trajectory of PITT winds under the real historical radiative forcing and tropical Pacific SST evolution. This ensemble mean is arguably the best available reconstruction of historical PITT winds, since it averages over multiple realisations of the unknown internal climate variability associated with regions outside the tropical Pacific. Model correlation maps (Supplementary Figure S5) confirm that the PACE ensemble-mean winds follow the processes seen in the observations.

The PACE ensemble mean PITT winds show a general eastward trend, with eastward wind anomalies in 1940, the 1950s, 1970, and 1980 onwards (Figure 3a) that are consistent with the glacial history inferred from sediments[12] and remote sensing observations[3,4,8]. These linked wind and glacial anomalies are explored further below. The wind history is also supported by water-isotope ratios from West Antarctic ice cores, which show an increasing trend during the 20$^{th}$ century and anomalously high values in response to the major El Niño of the early 1940s (refs. [28,29]).

**The role of anthropogenic forcing**

The PACE ensemble mean contains both a radiatively-forced trend and the mean influence of internal variability associated with the tropical Pacific. We separate these by estimating the radiatively-forced trend from the CESM Large Ensemble[30] (LENS; Methods). LENS uses the same model as PACE but without tropical SST restoring, providing 40 different realisations of

internal climate variability from all sources, Pacific and otherwise (Figure 3c). Taking the ensemble mean of LENS averages out this random internal variability, isolating the radiatively forced trend. The LENS ensemble mean has a PITT zonal wind trend of ~0.5 m/s/century during 1920—2005 (Table 1). Taken together, the CESM simulations (LENS and PACE) therefore imply that a forced wind trend removed a mean easterly PITT wind of ~0.5 m/s that existed during the 1920s, to arrive at the present near-zero mean zonal winds (Figure 3a). Acceleration of the southern sub-polar westerlies is a well-known consequence of the meridional structure of radiatively forced atmospheric warming[31,32]. Our results show that this trend includes the latitude of PITT winds (Figure 4a), despite the low correlation between the sub-polar westerlies and PITT winds on interannual timescales (see the Southern Annular Mode in Supplementary Figures S2 and S4).

The PITT region is highly sensitive to the modelled pattern of trends in the sub-polar westerlies[31]. The wider ensemble of climate models contributing to the Coupled Model Intercomparison Project, phase 5 (CMIP5; Methods) includes a variety of historical trends. The CMIP5 ensemble has no mean trend (Table 1), so the CESM is an outlier in this regard. However, the CMIP5 simulations have large biases in mean PITT winds relative to ERA-Interim (Figure 4b, Supplementary Table S1), and the simulations with a smaller bias have a larger historical trend. The CESM simulations have an exceptionally small bias in mean PITT winds, providing support for their relatively large historical trends.

To formally separate tropical Pacific variability from the radiatively-forced trend, we combine the PACE and LENS ensembles. As described above, the LENS ensemble mean represents the radiatively-forced trend, while the PACE ensemble mean represents the radiatively-forced

144 trend plus the real tropical Pacific variability. Therefore, to isolate the influence of Pacific
145 variability, we subtract the LENS ensemble mean ('forced response') from the PACE ensemble
146 mean ('full response') to leave the 'tropical response'[27], i.e. the influence of tropical Pacific
147 SST restoring (Figure 3b). Tropical response winds closely follow the unfiltered IPO index
148 (Methods), implying multi-decadal variability in PITT winds (e.g. filtered IPO in Figure 3b) that
149 may be of great importance to the ongoing WAIS ice loss[7]. Comparing the PACE ensemble
150 mean to the tropical response further illustrates the impact of the forced trend. The variability
151 has not changed appreciably during the 20$^{th}$ century (Figure 3b), but absolute westerly wind
152 anomalies that were rare have become commonplace (Figure 3a). Given the strong evidence
153 for a positive relationship between zonal wind anomalies and CDW import, this implies that
154 warm anomalies in the Amundsen Sea have become progressively more prevalent through
155 the 20$^{th}$ century as a result of radiative forcing.
156
157 Radiative forcing has several sources, both anthropogenic (greenhouse gases, ozone,
158 aerosols, land use) and natural (volcanoes, solar). The LENS ensemble mean represents the
159 net effect of all sources, and additional simulations would be required to formally isolate the
160 anthropogenic contribution. However, previous work has shown that forced trends in the
161 southern sub-polar westerlies are dominated by anthropogenic influences[33-35]. In contrast,
162 there is no conclusive evidence that Pacific variability has been significantly affected by
163 anthropogenic forcing[36,37]. Therefore, the evidence suggests that the forced trend in PITT
164 winds is primarily anthropogenic in origin, while the influence of the tropical Pacific is
165 primarily natural.
166
167 **Implications for the West Antarctic Ice Sheet**

168 This analysis of the climate model ensembles offers a plausible narrative for the ongoing WAIS
169 ice loss. i) In the 1920s, the WAIS was closer to balance with cooler Amundsen Sea conditions
170 associated with mean easterly PITT winds. ii) Through the 20th century, the mean easterlies
171 were progressively weakened by anthropogenic radiative forcing, causing tropically-forced
172 decadal warm ocean anomalies to become more prevalent at the ice-sheet margin. iii)
173 Episodes of particularly strong eastward wind anomalies, e.g. around 1940 (refs. [28,29]), created
174 strong melting anomalies that caused ice streams to un-ground from seabed ridges,
175 prompting progressive retreat as a result of ice and ocean feedbacks[10,11]. iv) As warm
176 anomalies became more prevalent in recent decades, the ice-sheet imbalance was
177 exacerbated, reaching the present-day rate.
178
179 Figure 5 illustrates this narrative by comparing PACE ensemble-mean winds to the
180 glaciological evidence. Prominent eastward wind anomalies around 1940 and 1970 are
181 consistent with the dates of initial and final ungrounding of Pine Island Glacier from a seabed
182 ridge inferred from sediment records and remote sensing[8,12]. Since 1980, eastward wind
183 anomalies have triggered accelerations in glacial discharge[3] that induced drawdown of inland
184 ice[4]. These eastward anomalies reflect Pacific variability that is not at all unusual in the record
185 (Figure 3b). However, when superimposed upon the anthropogenic trend this variability
186 produces periods of absolute westerly winds that are sufficiently anomalous to account for
187 much of the current ice loss.
188
189 This narrative proposes that present-day ice loss is driven by an anthropogenically-forced
190 melting imbalance modulated by natural tropical variability and ice—ocean feedbacks. The
191 WAIS lost mass during recent warm ocean anomalies, but did not gain mass during cool

anomalies[3,4,6,38], an asymmetry that is consistent with both ice—ocean feedbacks and with the ice sheet being historically in balance with cooler ocean conditions. However, we caution that other narratives cannot yet be discounted, including those based solely on long-term natural variability in ice sheet dynamics and climate forcing (e.g. the IPO).

The unknown timing and magnitude of internal variability – other than that related to the tropical Pacific – adds considerable uncertainty to the actual trend in PITT winds over the 20$^{th}$ century. All PACE simulations are equally plausible, and the standard deviation of PACE trends is nearly half the mean trend (Table 1, Supplementary Figure S6). In addition, the centennial trends are much smaller than decadal internal variability. In observations and CESM simulations, the ~0.5 m/s variability has equivalent magnitude to ~100 years of the mean forced trends (Table 1, Figure 3). Decadal internal variability therefore dominates ice sheet and ocean variability during the modern observational era (since 1979), and will continue to dominate observations for decades to come.

While weaker than decadal variability on short timescales, on centennial timescales we suggest that the wind trend is sufficiently large to have influenced ice-sheet stability. Recent Pine Island Glacier ice-shelf melting anomalies of ~40 Gt/y are associated with PACE ensemble mean wind anomalies of ~1.5 m/s (Figure 5). If this ratio held for centennial trends, the PACE mean trend of ~0.7 m/s/century would induce a melting trend of ~20 Gt/y/century. Integrated over 100 years, this is half the magnitude of the decadal melting anomalies that affect ice-sheet mass balance (Figure 5). Furthermore, Pine Island Glacier discharge was ~80 Gt/y in 1974 (ref. [3]). If half was accounted for by melting[39], the integrated centennial trend would represent a 50% increase in melting over the 1974 rate. This simple argument supports

the importance of the wind trends, but the centennial relationship between winds and melting remains a topic of considerable uncertainty that requires much further research.

**Future projections**

The historical PITT wind trend continues through the 21st century for the high-emissions RCP8.5 scenario, with LENS and CMIP5 projecting a mean trend of ~0.4 m/s/century (Table 1; Figures 3 and 4c). This suggests that warmer Amundsen Sea conditions will become progressively more prevalent. By 2100 the mean westerly is comparable to 1 standard deviation of the internal variability, so the wind is reliably westerly (Table 1). The total 1920—2100 wind change is equivalent to ~2 standard deviations of the internal variability, so if the WAIS were close to balance with ocean conditions in the 1920s, this suggests substantial ice-sheet change by 2100.

As described above, radiative forcing impacts in this region are dominated by anthropogenic influences, primarily ozone depletion and greenhouse gases[33-35]. Thirty-year wind trends within the CESM centennial records (Supplementary Figure S7) show elevated trends centred on the 1980s and reduced trends centred on 2030 that represent the influence of ozone depletion and recovery. In the RCP8.5 scenario, the effect of ozone depletion causes only a temporary perturbation to the underlying trend, caused by greenhouse gases, that persists throughout the 20th and 21st centuries.

Of course, 21st century radiative forcing is not decided. Under RCP4.5, CMIP5 simulations project PITT wind trends that are not significantly different from zero (Table 1, Figures 3d and 4c; Supplementary Figure S6) because ozone recovery fully compensates the weaker

240 greenhouse-gas forcing in this scenario[40]. The difference between CMIP5 RCP4.5 and RCP8.5
241 wind trends is significant at the 95% confidence level (Supplementary Tables S2 and S3).
242 Alternative evidence can be gained by comparing the LENS RCP8.5 projection to the CESM
243 'medium ensemble' (MENS; ref. [41]), a 15-member ensemble of RCP4.5 projections (Methods).
244 The 2006-2080 MENS mean projected wind trend is lower than that of LENS, but unlike the
245 CMIP5 results this difference is not statistically significant (Supplementary Tables S2 and S3).
246
247 The CMIP5 RCP4.5/8.5 comparison samples a range of model responses to radiative forcing,
248 while the LENS/MENS comparison better characterises the role of internal variability, in a
249 model with exceptionally low mean-state bias. Overall, these results suggest that weaker
250 wind trends under RCP4.5 lead to Amundsen Sea ocean conditions frequently cooler than
251 under RCP8.5. RCP4.5 and RCP8.5 scenarios differ in a specific sub-set of anthropogenic
252 forcings (greenhouse gases, aerosols, land use), suggesting that policymakers have an
253 opportunity to 'weight the dice' towards a lower future sea-level contribution from the WAIS.
254 This conclusion relates to ocean changes induced by wind forcing, the mode of variability that
255 has dominated observations[5,6]. The future contribution of additional warming mechanisms,
256 such as a general warming of the CDW entering the Amundsen Sea, is highly uncertain[42].
257
258 Owing to the unpredictable phasing of internal climate variability, there is significant variance
259 in wind trends between ensemble members, with the one-standard-deviation range for LENS
260 and MENS extending between no trend and twice the mean trend (Supplementary Figure S6).
261 Internal variability is therefore of comparable importance to radiative forcing in determining
262 the magnitude of PITT wind changes during the 21$^{st}$ century. In the CMIP5 ensembles, inter-
263 model differences add further uncertainty to the future trajectory of PITT winds

(Supplementary Figure S6). To deliver meaningful projections of the WAIS over this period, ice sheet models will need to adopt an ensemble approach forced by multiple realisations of ocean melting.

**Data Availability**

Sea ice concentration and drift data that support the findings of this study are available from the National Snow and Ice Data Center (https://doi.org/10.5067/8GQ8LZQVL0VL and https://doi.org/10.5067/O57VAIT2AYYY respectively). ERA-Interim reanalysis data are available from the European Centre for Medium-Range Weather Forecasts (https://apps.ecmwf.int/datasets/data/interim-full-daily). Extended Reconstructed Sea-surface Temperature data are available from the National Oceanic and Atmospheric Administration National Climatic Data Center (https://www.ncdc.noaa.gov/data-access/marineocean-data/extended-reconstructed-sea-surface-temperature-ersst-v5). Seabed data are available from the British Antarctic Survey (https://secure.antarctica.ac.uk/data/bedmap2). Climate indices are available from the National Oceanic and Atmospheric Administration Earth System Research Laboratory (https://www.esrl.noaa.gov/psd/data/climateindices/list). CMIP5 simulation data are available from the Centre for Environmental Data Analysis (http://www.ceda.ac.uk). CESM simulation data are available from the National Center for Atmospheric Research Climate Data Gateway (https://www.earthsystemgrid.org).

**Code Availability**

The Matlab scripts used for the analyses described in this study can be obtained from the corresponding author upon reasonable request.

## References


1 Shepherd, A. *et al.* Mass balance of the Antarctic Ice Sheet from 1992 to 2017. *Nature* **558**, 219-222, doi:10.1038/s41586-018-0179-y (2018).

2 Shepherd, A., Wingham, D. & Rignot, E. Warm ocean is eroding West Antarctic Ice Sheet. *Geophys Res Lett* **31**, L23402, doi:10.1029/2004gl021106 (2004).

3 Mouginot, J., Rignot, E. & Scheuchl, B. Sustained increase in ice discharge from the Amundsen Sea Embayment, West Antarctica, from 1973 to 2013. *Geophys Res Lett* **41**, 1576-1584, doi:10.1002/2013gl059069 (2014).

4 Konrad, H. *et al.* Uneven onset and pace of ice-dynamical imbalance in the Amundsen Sea Embayment, West Antarctica. *Geophys Res Lett*, 910-918, doi:10.1002/2016GL070733 (2017).

5 Jenkins, A. *et al.* Decadal ocean forcing and Antarctic Ice Sheet response: Lessons from the Amundsen Sea. *Oceanography* **29**, 106-117, doi:10.5670/oceanog.2016.103 (2016).

6 Jenkins, A. *et al.* West Antarctic Ice Sheet retreat in the Amundsen Sea driven by decadal oceanic variability. *Nat Geosci* **11**, 733-738, doi:10.1038/s41561-018-0207-4 (2018).

7 Snow, K. *et al.* The Response of Ice Sheets to Climate Variability. *Geophys Res Lett* **44**, 11878-11885, doi:10.1002/2017gl075745 (2017).

8 Jenkins, A. *et al.* Observations beneath Pine Island Glacier in West Antarctica and implications for its retreat. *Nat Geosci* **3**, 468-472, doi:10.1038/Ngeo890 (2010).

9 Steig, E. J., Ding, Q., Battisti, D. S. & Jenkins, A. Tropical forcing of Circumpolar Deep Water Inflow and outlet glacier thinning in the Amundsen Sea Embayment, West Antarctica. *Annals of Glaciology* **53**, 19-28, doi:10.3189/2012AoG60A110 (2012).

10 De Rydt, J., Holland, P. R., Dutrieux, P. & Jenkins, A. Geometric and oceanographic controls on melting beneath Pine Island Glacier. *J Geophys Res-Oceans* **119**, 2420-2438, doi:10.1002/2013JC009513 (2014).

11 De Rydt, J. & Gudmundsson, G. H. Coupled ice shelf-ocean modeling and complex grounding line retreat from a seabed ridge. *Journal of Geophysical Research-Earth Surface* **121**, 865-880, doi:10.1002/2015jf003791 (2016).

12 Smith, J. A. *et al.* Sub-ice-shelf sediments record history of twentieth-century retreat of Pine Island Glacier. *Nature* **541**, 77-80, doi:10.1038/nature20136 (2016).

13 Jacobs, S. S., Hellmer, H. H. & Jenkins, A. Antarctic ice sheet melting in the Southeast Pacific. *Geophys Res Lett* **23**, 957-960 (1996).

14 Dutrieux, P. *et al.* Strong Sensitivity of Pine Island Ice-Shelf Melting to Climatic Variability. *Science* **343**, 174-178, doi:10.1126/science.1244341 (2014).

15 Thoma, M., Jenkins, A., Holland, D. & Jacobs, S. Modelling Circumpolar Deep Water intrusions on the Amundsen Sea continental shelf, Antarctica. *Geophys Res Lett* **35**, L18602, doi:10.1029/2008gl034939 (2008).

16 Kimura, S. *et al.* Oceanographic Controls on the Variability of Ice-Shelf Basal Melting and Circulation of Glacial Meltwater in the Amundsen Sea Embayment, Antarctica. *J Geophys Res-Oceans* **122**, 10131-10155, doi:10.1002/2017jc012926 (2017).

17 Webber, B. G. M., Heywood, K. J., Stevens, D. P. & Assmann, K. M. The Impact of Overturning and Horizontal Circulation in Pine Island Trough on Ice Shelf Melt in the Eastern Amundsen Sea. *Journal of Physical Oceanography* **49**, 63-83, doi:10.1175/Jpo-D-17-0213.1 (2019).

18 Assmann, K. M. *et al.* Variability of Circumpolar Deep Water transport onto the Amundsen Sea continental shelf through a shelf break trough. *J Geophys Res-Oceans* **118**, 6603-6620, doi:10.1002/2013jc008871 (2013).

19 Walker, D. P., Jenkins, A., Assmann, K. M., Shoosmith, D. R. & Brandon, M. A. Oceanographic observations at the shelf break of the Amundsen Sea, Antarctica. *J Geophys Res-Oceans* **118**, 2906-2918, doi:10.1002/Jgrc.20212 (2013).

20 St-Laurent, P., Klinck, J. M. & Dinniman, M. S. Impact of local winter cooling on the melt of Pine Island Glacier, Antarctica. *J Geophys Res-Oceans* **120**, 6718-6732, doi:10.1002/2015JC010709 (2015).
21 Davis, P. E. D. *et al.* Variability in Basal Melting Beneath Pine Island Ice Shelf on Weekly to Monthly Timescales. *J Geophys Res-Oceans* **123**, 8655-8669, doi:10.1029/2018jc014464 (2018).
22 Webber, B. G. M. *et al.* Mechanisms driving variability in the ocean forcing of Pine Island Glacier. *Nat Commun* **8**, 14507, doi:10.1038/ncomms14507 (2017).
23 Kim, T. W. *et al.* Is Ekman pumping responsible for the seasonal variation of warm Circumpolar Deep Water in the Amundsen Sea? *Continental Shelf Research* **132**, 38-48, doi:10.1016/j.csr.2016.09.005 (2017).
24 Raphael, M. N. *et al.* The Amundsen Sea Low: Variability, Change, and Impact on Antarctic Climate. *Bulletin of the American Meteorological Society* **97**, 111-121, doi:10.1175/Bams-D-14-00018.1 (2016).
25 Lachlan-Cope, T. & Connolley, W. Teleconnections between the tropical Pacific and the Amundsen-Bellinghausens sea: Role of the El Nino Southern Oscillation. *Journal of Geophysical Research-Atmospheres* **111**, D23101, doi:10.1029/2005jd006386 (2006).
26 Deser, C., Alexander, M. A., Xie, S. P. & Phillips, A. S. Sea Surface Temperature Variability: Patterns and Mechanisms. *Annual Review of Marine Science* **2**, 115-143, doi:10.1146/annurev-marine-120408-151453 (2010).
27 Schneider, D. P. & Deser, C. Tropically driven and externally forced patterns of Antarctic sea ice change: reconciling observed and modeled trends. *Climate Dynamics* **50**, 4599-4618, doi:10.1007/s00382-017-3893-5 (2018).
28 Steig, E. J. *et al.* Recent climate and ice-sheet changes in West Antarctica compared with the past 2,000 years. *Nat Geosci* **6**, 372-375, doi:10.1038/Ngeo1778 (2013).
29 Schneider, D. P. & Steig, E. J. Ice cores record significant 1940s Antarctic warmth related to tropical climate variability. *Proceedings of the National Academy of Sciences of the United States of America* **105**, 12154-12158, doi:10.1073/pnas.0803627105 (2008).
30 Kay, J. E. *et al.* The Community Earth System Model (CESM) Large Ensemble Project: A Community Resource for Studying Climate Change in the Presence of Internal Climate Variability. *Bulletin of the American Meteorological Society* **96**, 1333-1349, doi:10.1175/Bams-D-13-00255.1 (2015).
31 Bracegirdle, T. J., Turner, J., Hosking, J. S. & Phillips, T. Sources of uncertainty in projections of 21st century westerly wind changes over the Amundsen Sea, West Antarctica, in CMIP5 climate models. *Climate Dynamics* **43**, 2093-2104, doi:10.1007/s00382-013-2032-1 (2014).
32 Harvey, B. J., Shaffrey, L. C. & Woollings, T. J. Equator-to-pole temperature differences and the extra-tropical storm track responses of the CMIP5 climate models. *Climate Dynamics* **43**, 1171-1182, doi:10.1007/s00382-013-1883-9 (2014).
33 Arblaster, J. M. & Meehl, G. A. Contributions of external forcings to southern annular mode trends. *J Climate* **19**, 2896-2905, doi:10.1175/Jcli3774.1 (2006).
34 Schneider, D. P., Deser, C. & Fan, T. T. Comparing the Impacts of Tropical SST Variability and Polar Stratospheric Ozone Loss on the Southern Ocean Westerly Winds. *J Climate* **28**, 9350-9372, doi:10.1175/Jcli-D-15-0090.1 (2015).
35 Gillett, N. P., Fyfe, J. C. & Parker, D. E. Attribution of observed sea level pressure trends to greenhouse gas, aerosol, and ozone changes. *Geophys Res Lett* **40**, 2302-2306, doi:10.1002/grl.50500 (2013).
36 Yeh, S. W. *et al.* ENSO Atmospheric Teleconnections and Their Response to Greenhouse Gas Forcing. *Rev Geophys* **56**, 185-206, doi:10.1002/2017rg000568 (2018).
37 Cai, W. J. *et al.* ENSO and greenhouse warming. *Nat Clim Change* **5**, 849-859, doi:10.1038/Nclimate2743 (2015).

38 Christianson, K. *et al.* Sensitivity of Pine Island Glacier to observed ocean forcing. *Geophys Res Lett* **43**, 10817-10825, doi:10.1002/2016gl070500 (2016).

39 Rignot, E., Jacobs, S., Mouginot, J. & Scheuchl, B. Ice-Shelf Melting Around Antarctica. *Science* **341**, 266-270, doi:10.1126/science.1235798 (2013).

40 Barnes, E. A., Barnes, N. W. & Polvani, L. M. Delayed Southern Hemisphere Climate Change Induced by Stratospheric Ozone Recovery, as Projected by the CMIP5 Models. *J Climate* **27**, 852-867, doi:10.1175/Jcli-D-13-00246.1 (2014).

41 Sanderson, B. M., Oleson, K. W., Strand, W. G., Lehner, F. & O'Neill, B. C. A new ensemble of GCM simulations to assess avoided impacts in a climate mitigation scenario. *Climatic Change* **146**, 303-318, doi:10.1007/s10584-015-1567-z (2018).

42 Little, C. M. & Urban, N. M. CMIP5 temperature biases and 21st century warming around the Antarctic coast. *Annals of Glaciology* **57**, 69-78, doi:10.1017/aog.2016.25 (2016).

43 Cavalieri, D. J., Parkinson, C. L., Gloersen, P. & Zwally, H. J. Sea Ice Concentrations from Nimbus-7 SMMR and DMSP SSM/I-SSMIS Passive Microwave Data, Version 1. 1992-2016. (National Snow and Ice Data Center, Boulder, Colorado, USA, 1996).

44 Tschudi, M., Fowler, C., Maslanik, J., Stewart, J. S. & Meier, W. Polar Pathfinder Daily 25 km EASE-Grid Sea Ice Motion Vectors, Version 3. 1992-2016. (National Snow and Ice Data Center, Boulder, Colorado, USA., 2016).

45 Dee, D. P. *et al.* The ERA-Interim reanalysis: configuration and performance of the data assimilation system. *Quarterly Journal of the Royal Meteorological Society* **137**, 553-597, doi:10.1002/Qj.828 (2011).

46 Fretwell, P. *et al.* Bedmap2: improved ice bed, surface and thickness datasets for Antarctica. *The Cryosphere* **7**, 375-393, doi:10.5194/tc-7-375-2013 (2013).

47 Huang, B. *et al.* NOAA Extended Reconstructed Sea Surface Temperature (ERSST). Version 5. 1854-2016. (NOAA National Centers for Environmental Information, 2017).

48 Crosby, D. S., Breaker, L. C. & Gemmill, W. H. A Proposed Definition for Vector Correlation in Geophysics - Theory and Application. *Journal of Atmospheric and Oceanic Technology* **10**, 355-367 (1993).

49 Kim, C. S. *et al.* Variability of the Antarctic Coastal Current in the Amundsen Sea. *Estuarine Coastal and Shelf Science* **181**, 123-133, doi:10.1016/j.ecss.2016.08.004 (2016).

50 Mazur, A. K., Wåhlin, A. K. & Krezel, A. An object-based SAR image iceberg detection algorithm applied to the Amundsen Sea. *Remote Sensing of Environment* **189**, 67-83, doi:10.1016/j.rse.2016.11.013 (2017).

51 Zhang, Y., Wallace, J. M. & Battisti, D. S. ENSO-like interdecadal variability: 1900-93. *J Climate* **10**, 1004-1020, doi:10.1175/1520-0442(1997)010<1004:Eliv>2.0.Co;2 (1997).

52 Power, S., Casey, T., Folland, C., Colman, A. & Mehta, V. Inter-decadal modulation of the impact of ENSO on Australia. *Climate Dynamics* **15**, 319-324, doi:10.1007/s003820050284 (1999).

53 Newman, M. *et al.* The Pacific Decadal Oscillation, Revisited. *J Climate* **29**, 4399-4427, doi:10.1175/Jcli-D-15-0508.1 (2016).

54 Henley, B. J. *et al.* A Tripole Index for the Interdecadal Pacific Oscillation. *Climate Dynamics* **45**, 3077-3090, doi:10.1007/s00382-015-2525-1 (2015).

55 Bretherton, C. S., Widmann, M., Dymnikov, V. P., Wallace, J. M. & Blade, I. The effective number of spatial degrees of freedom of a time-varying field. *J Climate* **12**, 1990-2009, doi:10.1175/1520-0442(1999)012<1990:Tenosd>2.0.Co;2 (1999).

56 Deser, C., Guo, R. X. & Lehner, F. The relative contributions of tropical Pacific sea surface temperatures and atmospheric internal variability to the recent global warming hiatus. *Geophys Res Lett* **44**, 7945-7954, doi:10.1002/2017gl074273 (2017).

57 Kosaka, Y. & Xie, S. P. Recent global-warming hiatus tied to equatorial Pacific surface cooling. *Nature* **501**, 403-407, doi:10.1038/nature12534 (2013).

58 Kosaka, Y. & Xie, S. P. The tropical Pacific as a key pacemaker of the variable rates of global warming. *Nat Geosci* **9**, 669-673, doi:10.1038/Ngeo2770 (2016).

**Acknowledgements**

We are grateful to the originators of the many open-access datasets synthesised in this study, including remotely-sensed sea ice data, atmospheric reanalysis model results, sea-surface temperature and bathymetry observations, derived climate indices, and many climate model simulations. PD was supported by NSF awards 1643285 and 1644159. EJS was supported by NSF award 1602435.

**Author Contributions**

PH conceived the study and led the data processing. TB processed the CMIP5 model results. All authors discussed the results and implications and collaborated on writing the manuscript at all stages.

**The authors declare no competing interests.**

**Corresponding Author**

Correspondence to P. Holland (p.holland@bas.ac.uk)

## Methods

### Observational datasets

The total surface stress formulae employ daily ice concentration[43] and drift[44] data derived from passive microwave satellite data, and surface winds from the European Centre for

461 Medium-Range Weather Forecasts ERA-Interim reanalysis[45]. The results are set in context
462 using the Bedmap2 seabed dataset[46]. The stress calculation is detailed below.
463
464 The variability of 10-m zonal winds and surface stresses in the Amundsen Sea are considered
465 over a PITT box extending from 115°-102° W, 71.8°-70.2° S (Figure 1). This box is focussed
466 upon the shelf-break mouths of the troughs feeding Pine Island and Thwaites glaciers, and is
467 therefore both further south and smaller than that used by other authors[5,6,9,14,15,31]. The box
468 used by these previous authors was chosen to reflect the coarser resolution of an earlier
469 reanalysis dataset[15]. These PITT winds are set in their wider context using global SST data from
470 the Extended Reconstructed SST (ERSST) v5 dataset[47], and global SLP from ERA-Interim.
471 Throughout the paper, the term 'eastward' is used to refer to wind anomalies oriented in the
472 eastward direction, while the term 'westerly' is used to refer to a wind that is actually blowing
473 from west to east in absolute terms.
474
475 **Calculation of surface stresses**
476 The 'total' surface stress ($\boldsymbol{\tau}$) is calculated simply as the sum of air—ocean ($\boldsymbol{\tau_a}$) and ice—ocean
477 ($\boldsymbol{\tau_i}$) stresses, weighted by ice concentration ($C$):
478 $$\boldsymbol{\tau} = (1 - C)\boldsymbol{\tau_a} + C\boldsymbol{\tau_i}.$$
479 The individual stresses are represented as
480 $$\boldsymbol{\tau_a} = \rho_a c_a |\boldsymbol{u_a}| \boldsymbol{u_a}$$
481 $$\boldsymbol{\tau_i} = \rho_o c_o |\boldsymbol{u_i}| \boldsymbol{u_i}$$
482 where $\boldsymbol{u_a}$ is the 10-m wind vector, $\boldsymbol{u_i}$ is the observed ice drift vector, $\rho_a$=1.3 kg/m$^3$ and $\rho_o$=1030
483 kg/m$^3$ are air and ocean densities, and $c_a$=0.001 and $c_o$=0.006 are air and ocean drag
484 coefficients.

This formulation is perhaps the simplest conceivable. There are many alterations that could be adopted[23], such as including the ocean surface current, adopting an air-ocean stress formulation that accounts for sea state, or attempting to represent spatial and temporal variation in drag coefficients. These alternatives are not pursued because their requirement for additional unknown quantities implies they may not lead to a more realistic stress. In particular, including ocean currents in the stress calculation could radically alter the results[16], but suitable current observations are not available. Our approach should be regarded as a simple first attempt to examine nominal total stresses in order to build understanding of the role of sea ice.

Ekman pumping by the total and wind-only stresses are calculated according to

$$w\boldsymbol{k} = \frac{\boldsymbol{\nabla} \times \boldsymbol{\tau}}{\rho_o f}$$

$$w_a\boldsymbol{k} = \frac{\boldsymbol{\nabla} \times \boldsymbol{\tau_a}}{\rho_o f}$$

where $\boldsymbol{k}$ is the vertical unit vector and $f$=-1.4×10$^{-4}$ s$^{-1}$ is the Coriolis parameter.

The above formulae employ daily ice concentration and drift data and reanalysis model winds. All datasets are used for 1992—2016, the period during which consistent passive microwave data are available, and are binned/interpolated to a 25 km resolution polar stereographic grid, upon which stresses are calculated. The stresses are smoothed spatially with a 3×3 grid cell mean to remove gridding artefacts manifested in the Ekman pumping fields. The vector correlation between total and wind-only stresses is calculated according to a technique that measures covariance in both magnitude and direction[48].

Anomalies in the wind-only stress and total stress have a complex relationship on-shelf (Supplementary Figure S1). Their correlation drops near coasts because the ice strength resists convergence and shear. However, there are also significant polynyas on-shelf, where mobile ice permits a higher stress[23,49] that is better correlated to winds. The largest is the Amundsen Sea Polynya, which forms in the lee of icebergs grounded on a ridge north of Bear Island[50]. Shearing of mobile polynya ice against pack ice to the north-east creates Ekman upwelling[23,49]. Similar features occur west of Siple Island and Grant Island, which also host grounded icebergs[50]. Accounting for sea ice strongly affects the Ekman pumping. Ekman pumping is generally weak, with interannual variability of only ~5 m/y, suggesting that it cannot account for the large variations of CDW layer thickness that govern melting[6,14]. Therefore, we focus upon variations in CDW import to the shelf driven directly by zonal stress anomalies at the shelf break[5,18,19]. Accounting for sea ice has little effect on zonal stress anomalies at the shelf break, so zonal winds are used as a proxy for zonal stress at the shelf break throughout the study.

**Climate indices**

The linkage between Amundsen Sea winds and a broad range of climatic indices (https://www.esrl.noaa.gov/psd/data/climateindices/list/) are considered, but the SOI and IPO are particularly emphasised. All measures of ENSO and Pacific decadal variability are correlated so the choice is not of crucial importance; the two chosen indices are most highly correlated with PITT winds (Supplementary Figure S4).

The SOI (http://www.cpc.ncep.noaa.gov/data/indices/soi) is a measure of ENSO variability. It is derived from the sea-level pressure difference between Tahiti and Australia (Figure 3c), a measure of anomalous atmospheric convection over the tropical Pacific. The SOI is positive during La Niña conditions, so we consider –SOI in order to align the index with the other measures considered.

The tripole IPO index (https://www.esrl.noaa.gov/psd/data/timeseries/IPOTPI/) is a measure of decadal variability in the Pacific climate system. This variability resembles ENSO but acts on longer timescales, features a different spatial pattern, and involves a variety of climate processes[51-53]. Pacific decadal variability has been characterised in several ways, for example as the second principal component (PC2) of monthly Pacific SST anomalies after a 13-year low-pass filter (PC1 being global warming)[54]. The 'tripole' index employed here uses the SST anomaly between three areas of the tropical and subtropical Pacific (Figure 2d) to represent the pattern of the associated Empirical Orthogonal Function and thus can be used to approximate the PC[54]. This index can be considered monthly (unfiltered), or subjected to a 13-year low-pass filter to recover decadal variability similar to that of the original PC. The unfiltered index represents the monthly variability that underlies the decadal variability.

**Significance of time series correlations**

Several figures involve the calculation of correlations between timeseries. These correlations are calculated on detrended time series at zero lag, after the application of a 2-year running mean. Owing to the use of a 2-year running mean throughout this study, the effective number of degrees of freedom in these correlations is relatively small for the 1979-2017 period used in Figures 2, S3, and S4. The effective sample size was analysed, accounting for

555 autocorrelation[55], and in all cases was found to be very close to Y/2, where Y is the number
556 of years in the record. This is the expected result for timeseries subjected to a 2-year running
557 mean that have negligible autocorrelation on timescales longer than 2 years. Therefore, we
558 derive the statistical significance of the correlations using a 2-sided t-test with Y/2 as the
559 degrees of freedom.
560
561 **Climate model simulations**
562 We examine Amundsen Sea winds in climate model simulations, including the Coupled Model
563 Intercomparison Project 5 (CMIP5) archive[31], the Community Earth System Model (CESM)
564 Large Ensemble (LENS)[30], CESM Medium Ensemble (MENS)[41], and CESM tropical Pacific
565 'pacemaker' simulations (PACE)[56]. CMIP5 data were obtained from the Centre for
566 Environmental Data Analysis (http://www.ceda.ac.uk/), while the CESM simulations were
567 obtained from the National Center for Atmospheric Research Climate Data Gateway
568 (https://www.earthsystemgrid.org/). The ensembles used are summarised in Supplementary
569 Table S1.
570
571 For the ensemble of CMIP5 simulations, the models and processing follow an earlier study[31].
572 Data were assessed from 'historical' forcing simulations from 1920—2005 and future
573 projections using (Representative Concentration Pathway) RCP4.5 and RCP8.5 from 2006—
574 2100. We include only the first simulation from each different model to ensure the models
575 are weighted equally, totalling 30 (31) realisations of RCP4.5 (RCP8.5). The historical ensemble
576 includes the 31 simulations that continue to the RCP8.5 projection. RCP4.5 features a
577 radiative forcing that stabilises in 2100, while RCP8.5 represents a continually increasing
578 forcing. In both scenarios, stratospheric ozone recovers to near pre-ozone hole levels by 2100.

For each scenario, the spread between ensemble members reflects a combination of both model uncertainty and internal climate variability. By comparing the projected trends in the two ensembles, we are able to determine the influence of future radiative forcing upon PITT winds.

The LENS ensemble comprises 40 simulations of the CESM1.1 coupled climate model, in which the atmosphere, sea ice, and ocean models have a resolution of ~1° (ref. [30]). Each simulation represents the period 1920-2100, using 'historical' forcings until 2005 and RCP8.5 afterwards. The CESM and its direct ancestors are not included in the CMIP5 ensemble analysed here. The only difference between LENS ensemble members is a random machine-precision ($10^{-14}$ °C) perturbation to the initial atmospheric temperature, which rapidly grows in the chaotic climate system. Since the model physics are identical in all simulations, the spread between ensemble members represents only the influence of random internal climate variability.

The MENS ensemble comprises 15 simulations of the same model as LENS. MENS simulations are identical to LENS in every way apart from the projected radiative forcing, which follows RCP4.5 instead of RCP8.5. MENS simulations branch from the first 15 members of LENS in 2006, running until 2080. Comparing MENS and LENS reveals the influence of radiative forcing scenario upon PITT winds within the CESM model. This offers additional information to the CMIP5 comparison because the CESM model has exceptionally low bias, and the difference between ensemble members is caused only by internal climate variability, free from the influence of model structural difference.

602 One complication is that MENS simulations only run until 2080, rather than 2100 in the other
603 ensembles. Supplementary Tables S2 and S3 report LENS ensemble metrics for both the
604 period to 2080 and 2100, for ease of comparison to MENS. The LENS trends are larger over
605 the longer period, and their difference to MENS more significant. However, we have no way
606 of knowing how MENS would evolve after 2080, so in the main paper we rely upon the 2006-
607 2080 trends, for which the difference between LENS and MENS ensembles is not statistically
608 significant (Supplementary Table S3). This is partly a result of the relatively small size of MENS.
609
610 The PACE ensemble comprises 20 historical simulations (1920—2013) of the CESM1.1 model,
611 in which eastern tropical Pacific SSTs are constrained to follow their observed history[56]. The
612 restoring imposes SST anomalies in the region between 15°S-15°N and 180°W to the coast of
613 the Americas, plus a restoring ramp-down region of 5° to the north, south, and west[57]. The
614 restoring replaces model temporal SST anomalies with observed temporal SST anomalies.
615 Therefore, to a first approximation, the restoring does not alter any mean-state bias in the
616 climate model. The non-conservation of heat induced by the restoring is typically smaller than
617 both the top-of-atmosphere radiation imbalance, and its model ensemble spread[58]. PACE
618 simulations use historical forcings for 1920—2005 and RCP8.5 forcings for 2006—2013. The
619 models used in the LENS and PACE ensembles are structurally identical. The forcing of the two
620 ensembles is also identical apart from the representation of ozone depletion, which is derived
621 from different datasets in the two ensembles[27]. This difference in ozone forcing has some
622 effect on stratospheric temperatures, but no discernible effect upon the surface winds that
623 are the focus of this study[34]. This is evident from the absence of any noticeable signature of
624 ozone depletion in the tropical response (the mean difference between PACE and LENS; see
625 below) in Figure 3b. Since all PACE ensemble members have identical model structure and are

constrained to follow the observed history of eastern and central tropical Pacific SST anomalies, the spread between PACE ensemble members represents internal climate variability that is associated with SSTs outside this region.

**Interpretation of climate model results**

The real climate trajectory combines the effects of a single realisation of random internal climate variability with a response to external forcings (greenhouse gases, ozone, aerosols, land use, volcanoes, solar). Therefore it should be most comparable to an individual member from our ensembles. However, model representations of the climate system are imperfect. The value of our model ensembles is therefore in helping to distinguish the effects of forcing, internal variability, and model uncertainty.

The CMIP5 ensemble spread represents both model uncertainty and internal climate variability. The LENS and MENS ensemble spread represents only internal variability. The PACE ensemble spread represents only internal variability associated with regions outside the eastern tropical Pacific. The CMIP5, LENS, and MENS ensemble means are derived by averaging over multiple realisations of random internal climate variability, and therefore represent estimates of the climate response to external forcings. These estimates differ in that the CMIP5 ensemble mean includes model uncertainty in the forced response, while the LENS and MENS ensemble means more accurately estimate the forced response of a single model. The PACE ensemble mean estimates the combined effect of the forced response and the real variability associated with the observed trajectory of tropical Pacific SSTs.

649 The influence of Pacific variability on the historical PITT wind trend can be deduced from
650 differences between PACE and LENS. There are significant summer and autumn trends in both
651 ensembles, while only PACE has trends in winter and spring (Supplementary Table S2). As a
652 result, the PACE annual trend is higher than that of LENS (Table 1, Supplementary Figure S6).
653 This difference between PACE and LENS mean trends is significant at the 95% confidence level
654 for annual trends and for winter and spring (Supplementary Table S3), suggesting that Pacific
655 variability made a small but detectible enhancement to the radiatively forced trend during
656 the 20$^{th}$ century.
657
658 Since the PACE and LENS ensembles use the same model, their response to external forcing
659 should in principle be the same. Therefore, we define the LENS ensemble mean as
660 representing the 'forced response' in both the LENS and PACE ensembles. We may then
661 subtract the LENS ensemble mean from the PACE ensemble mean to isolate the 'tropical
662 response'[27]. This tropical response is an estimate of the unforced variability in the climate
663 system that is associated with tropical Pacific SSTs. The crucial advantage in this approach is
664 that it allows us to consistently compare the magnitude of climate responses (e.g. PITT winds)
665 to external forcing (forced response) and tropical Pacific variability (tropical response).
666 Tropical response winds closely follow the unfiltered IPO index (Figure 3b), clarifying the
667 causality of the linkage. When tropical Pacific SSTs are prescribed, PITT winds covary with the
668 whole-Pacific SST pattern that results (hence they vary with the unfiltered IPO index). Since
669 the unfiltered IPO index represents variability that underlies decadal variability upon filtering,
670 this implies that PITT winds follow the decadal variability of the IPO.
671

672 There are several caveats to the interpretation of the tropical response. First, the approach
673 assumes that the forced and tropical responses are linearly separable, thus neglecting the
674 role of external forcing upon tropical variability. Second, the LENS and PACE ensembles have
675 different ozone forcing, which could contaminate the tropical response, though the impact of
676 this difference on surface winds is known to be small[34], and our results support this (Figure
677 3b). Third, the forced response in the LENS and PACE ensembles may actually differ, since the
678 restoring in the latter alters the SST trend within the restoring region[58]. Ultimately, however,
679 the results of many studies show that the 'tropical response' concept realistically and usefully
680 depicts the influence of tropical Pacific variability[27].
681
682 **Amundsen Sea ice-shelf melting timeseries**
683 Figure 5 shows a timeseries of ice-shelf melt rates derived from ocean observations near Pine
684 Island Glacier (PIG)[5,14] and Dotson Ice Shelf (DIS)[6]. Including both ice shelves offers improved
685 temporal coverage, since most oceanographic surveys sampled only one of the two ice fronts.
686 While the two ice shelves occupy distinct seabed troughs, and differ in the details of their
687 geometry and oceanographic forcing, the phasing of their interannual variability is coherent
688 and thought to be driven by common shelf-break wind forcing[5,6,14,16]. The derivation of melt
689 rates for each ice shelf is fully documented in the original papers[6,14], and only their
690 combination requires further explanation here.
691
692 To display a consistent time series, we scale the DIS melt rates to produce an approximate
693 PIG-equivalent melt rate. The scaling is derived from three years which have melt rates for
694 both cavities (2009, 2012, 2014), which fortuitously includes the maximum and minimum

observed melt rates for both cavities. PIG-equivalent DIS melt rates are derived by regressing PIG melt rates against DIS melt rates for these three years, yielding

$$m_{PIGeq} = 23.9 + 0.54\, m_{DIS},$$

where all values are in Gt/y. These PIG-equivalent DIS melt rates are then combined with unscaled PIG melt rates to create the melt timeseries. The mean of the two melt values is used for years where both cavities were sampled. The combination of the two cavities is based upon only three common years and is therefore offered only for illustrative purposes. Nevertheless, the combined time series offers a credible account of decadal variability in the Amundsen Sea that is consistent with the independent ERA-Interim winds (Figure 5).

## Tables

| | Wind variability<br>standard deviation of residuals from linear trends<br>m/s | Wind trend<br>mean ± 1 s.d. of trends in ensemble members<br>m/s/century |
|---|---|---|
| ERA-Interim<br>1979-2016 | 0.49 | 0.04 |
| PACE historical<br>1920-2005 | 0.54 | **0.69 ± 0.27** |
| LENS historical<br>1920-2005 | 0.60 | **0.45 ± 0.35** |
| CMIP5 historical<br>1920-2005 | 0.49 | 0.05 ± 0.36 |
| MENS RCP4.5<br>2006-2080 | 0.59 | **0.24 ± 0.27** |
| LENS RCP8.5<br>2006-2100 | 0.58 | **0.38 ± 0.29** |
| CMIP5 RCP4.5<br>2006-2100 | 0.48 | 0.13 ± 0.47 |
| CMIP5 RCP8.5<br>2006-2100 | 0.48 | **0.36 ± 0.48** |

**Table 1: Variability and trends in Amundsen Sea winds in the climate model ensembles.** Variability in PITT winds is characterised by the standard deviation of residuals from the linear trends in all ensemble members. Note the timeseries have a 2-year running mean applied. Trends are characterised by the mean and standard deviation of the distribution of linear trends in the ensemble members. Mean trends in bold are significantly different from zero at the 99% confidence level under a one-sample t-test. CMIP5 historical and CMIP5 RCP4.5 projected mean trends are not significant at the 90% level.

## Figures

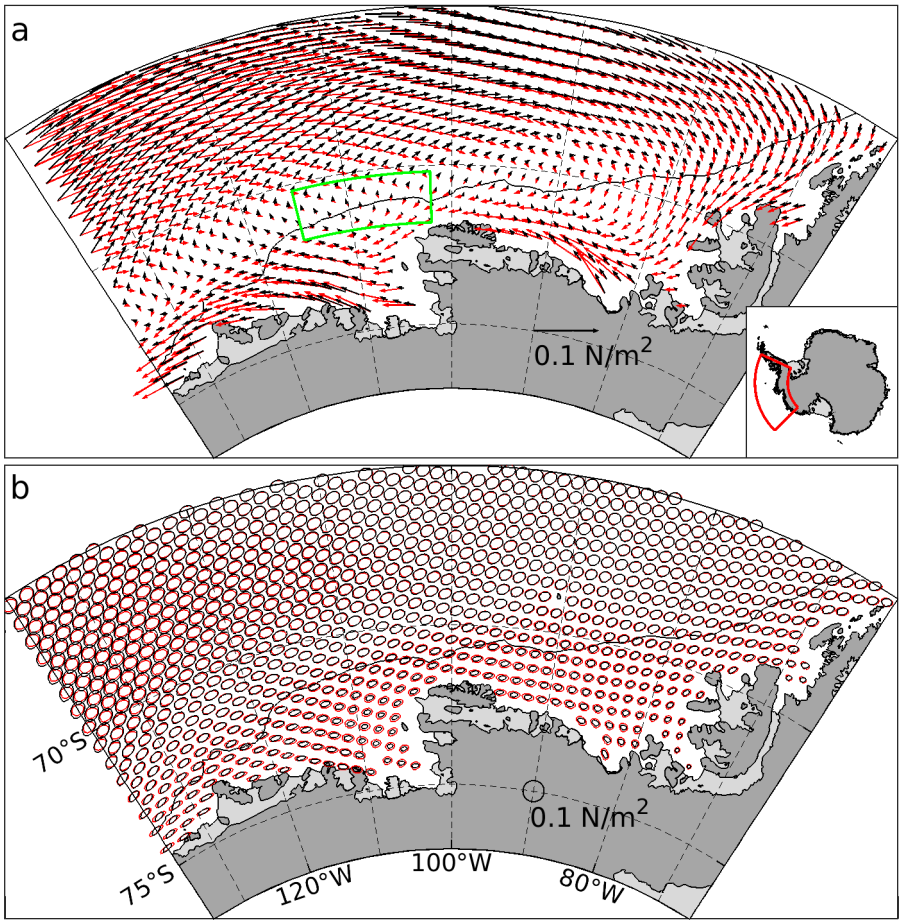


**Figure 1: Total surface stress and wind-only stress on the Amundsen Sea.** a) Mean 1992-2016 total stress (accounting for sea ice; black) and wind-only stress (red). b) Variance ellipses for monthly total and wind-only stress anomalies from seasonal climatology, aligned in the direction of maximum variance and scaled to 1 standard deviation. Vectors and ellipses are shown every second data point. The 1000 m depth contour at the shelf break is also shown. The green box shows the area of the Pine Island and Thwaites Troughs (PITT) at the shelf break, over which timeseries are calculated.

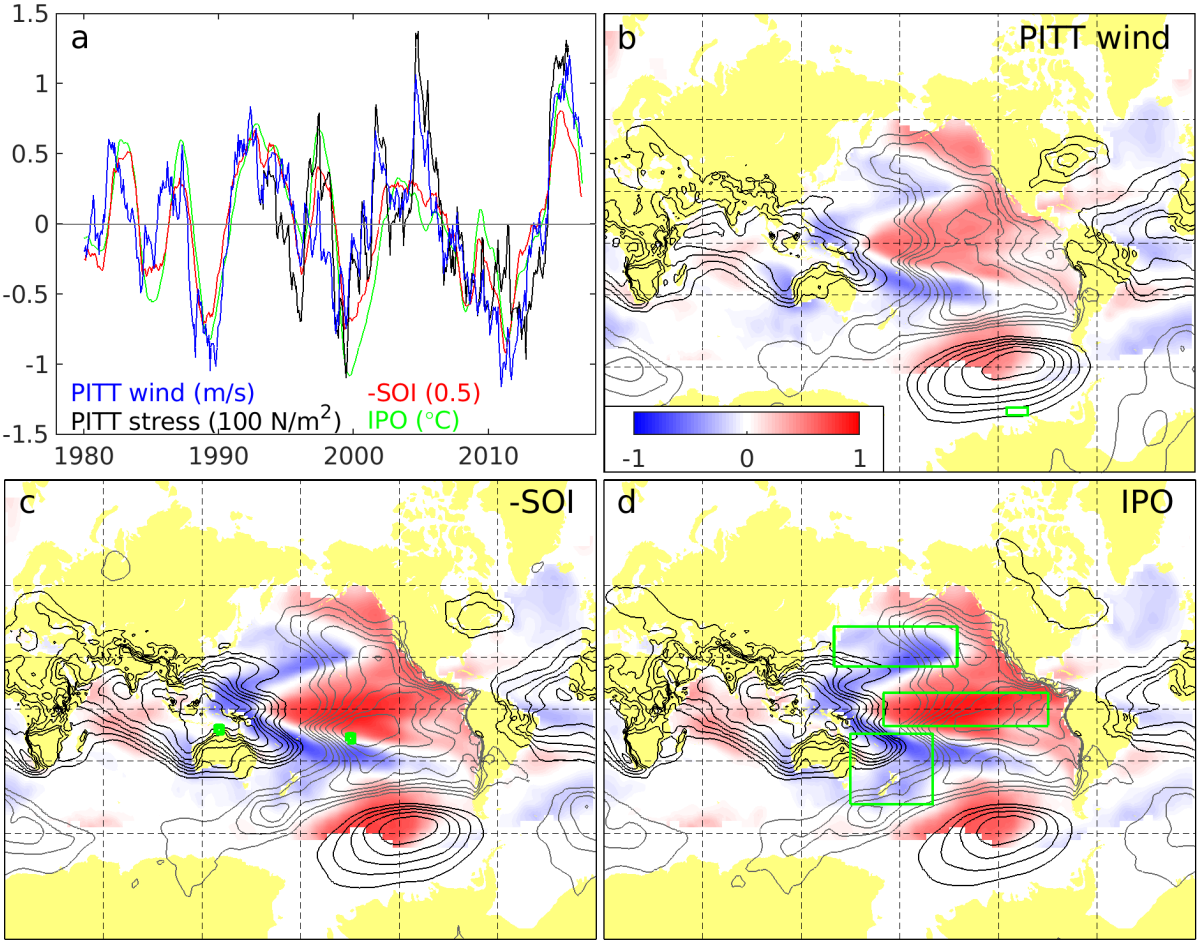


721

722 **Figure 2: Linkages between Amundsen Sea winds and global sea-surface temperature and**
723 **sea-level pressure.** a) Time series of zonal wind and zonal total stress over the PITT box, the
724 Southern Oscillation Index, and the Interdecadal Pacific Oscillation. The legend shows the
725 scaling for each timeseries. b-d) correlation maps of SST (colour) and SLP (contours) to PITT
726 winds and SOI and IPO indices. The maps show $r^2$ multiplied by the sign of the relationship.
727 SLP correlation contours have a spacing of 0.1, with black positive, grey negative, and the zero
728 contour omitted. The area of each index is shown in green.

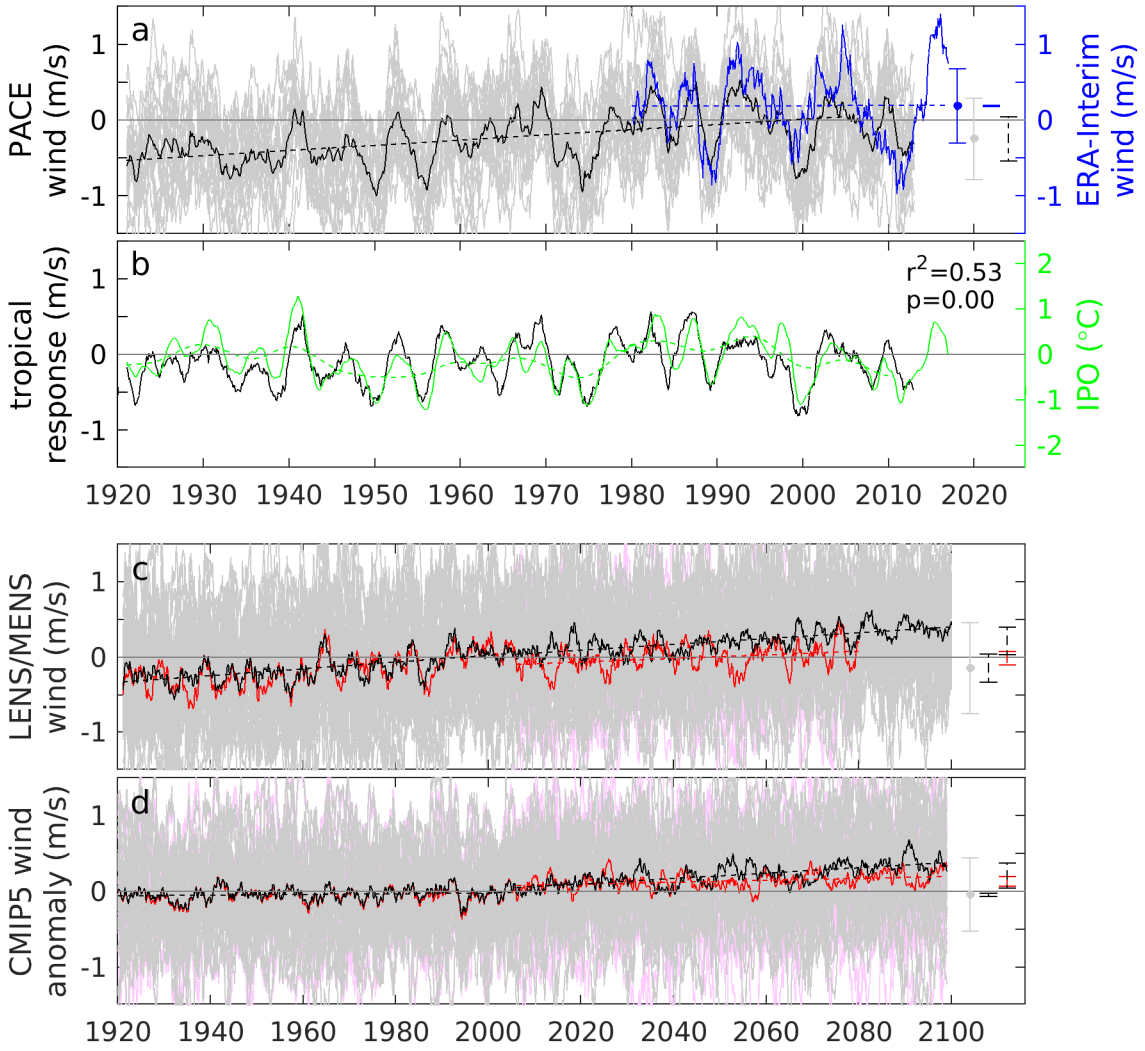


729

730 **Figure 3: Amundsen Sea winds within climate model ensembles.** a) Zonal winds over the
731 PITT box from ERA-Interim (blue), PACE simulations (grey), PACE ensemble mean (black) and
732 mean trend (dashed). b) 'tropical response' wind (black) and IPO index before (green) and
733 after (dashed) 13-year low-pass filter. c) Historical and projection simulations of LENS
734 (grey/black; RCP8.5) and MENS (pink/red; RCP4.5) ensembles. d) CMIP5 ensemble, including
735 RCP8.5 (grey/black) and RCP4.5 (pink/red). Error bars show the standard deviation of wind
736 anomalies (solid) and magnitude of historical and projected trends (dashed). CMIP5 models
737 contain large biases, so panel d shows anomalies from the 1979—2017 mean.

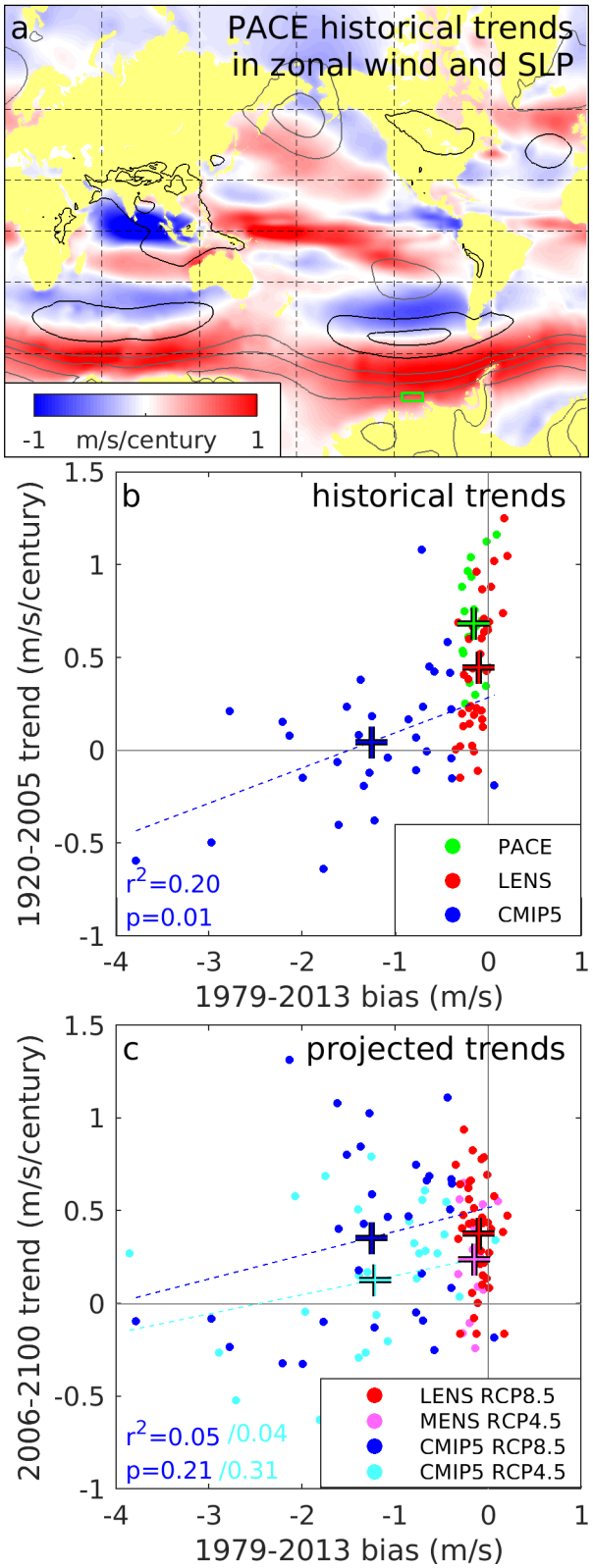


**Figure 4: Trends in Amundsen Sea winds within climate model ensembles.** a) 1920-2005 trends in the PACE ensemble mean. Colours (contours) show trend in zonal winds (SLP). Contours have a spacing of 0.5 hPa/century, with black positive, grey negative, and the zero contour omitted. b) historical and c) projected PITT wind trends versus present-day bias (mean model zonal wind minus mean ERA-Interim zonal wind). Ensemble-mean values are shown by a + symbol. The ensemble regression of CMIP5 historical trends shows that the larger LENS trend is consistent with its smaller bias. There is no dependence of CMIP5 projected trends upon present-day bias.

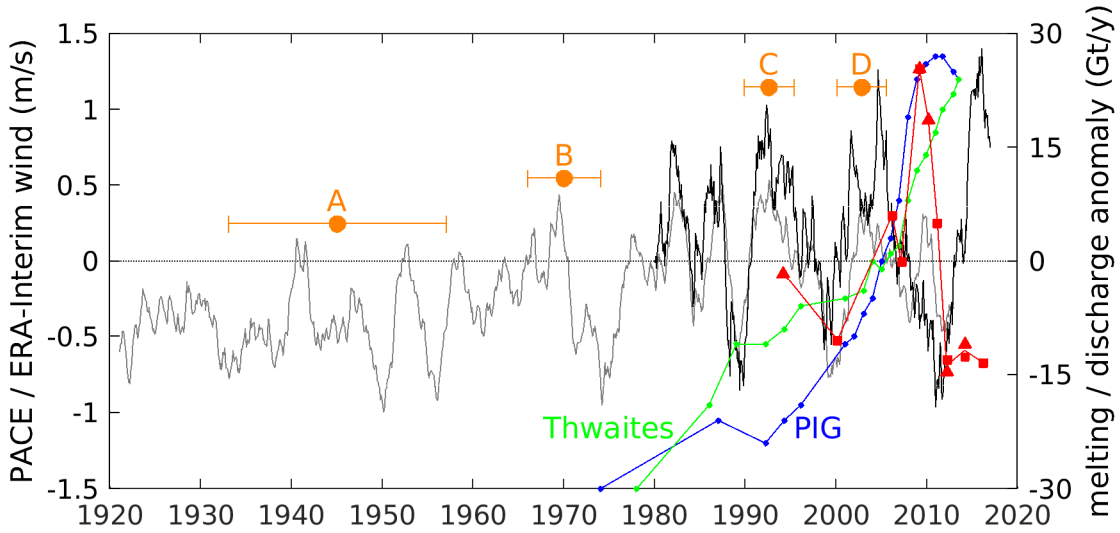


755

756 **Figure 5: One century of wind forcing and ice-sheet response.** Grey and black show PACE
757 ensemble-mean and ERA-Interim winds. Green and blue show anomalies in discharge of
758 Thwaites and Pine Island glaciers[3], relative to 102 and 108 Gt/y median values. Red shows
759 anomalies in combined melt rates from Pine Island Glacier[5] (triangles) and Dotson Ice Shelf[6]
760 (squares), relative to a median of 48 Gt/y. Orange events include initial (A) and final (B)
761 ungrounding of Pine Island Glacier from a submarine ridge[8,12], and the onset of recent
762 thinning of Pine Island (C) and Thwaites (D) glaciers[4] (mean ±1 s.d. of dates for tributaries).

## Supplementary Tables and Figures

| Name | Description and reference | Time period | Forcing | n | Wind bias (m/s) | | |
|---|---|---|---|---|---|---|---|
| | | | | | mean | s.d. | s.e. |
| PACE | CESM Pacific Pacemaker[56] | 1920-2013 | historical: radiative + tropical Pacific SSTs | 20 | -0.16 | 0.10 | 0.02 |
| MENS | CESM Medium Ensemble[41] | 1920-2080 | historical: radiative projected: RCP4.5 | 15 | -0.15 | 0.11 | 0.03 |
| LENS | CESM Large Ensemble[30] | 1920-2100 | historical: radiative projected: RCP8.5 | 40 | -0.11 | 0.13 | 0.02 |
| CMIP5 RCP4.5 | Coupled Model Intercomparison Project, phase 5 (ref. [31]) | 1920-2100 | historical: radiative projected: RCP4.5 | 31 | -1.21 | 0.86 | 0.16 |
| CMIP5 RCP8.5 | | 1920-2100 | historical: radiative projected: RCP8.5 | 30 | -1.26 | 0.86 | 0.16 |

Supplementary Table S1: Description of climate model ensembles considered in this study. The final three columns show statistics of the ensemble member wind biases, calculated relative to ERA-Interim during 1979-2013.

| | Summer DJF | Autumn MAM | Winter JJA | Spring SON | Annual |
|---|---|---|---|---|---|
| PACE historical 1920-2005 | **0.96 ± 0.47** | **0.57 ± 0.86** | **0.66 ± 0.60** | **0.60 ± 0.55** | **0.69 ± 0.27** |
| LENS historical 1920-2005 | **1.21 ± 0.61** | **0.48 ± 0.57** | 0.07 ± 0.59 | 0.18 ± 0.69 | **0.45 ± 0.35** |
| CMIP5 historical 1920-2005 | 0.02 ± 0.50 | 0.01 ± 0.74 | 0.03 ± 0.72 | 0.15 ± 0.58 | 0.05 ± 0.36 |
| MENS RCP4.5 2006-2080 | 0.03 ± 0.53 | **0.95 ± 0.87** | *-0.28 ± 0.61* | 0.35 ± 0.80 | **0.24 ± 0.27** |
| LENS RCP8.5 2006-2080 | 0.16 ± 0.64 | **1.14 ± 0.69** | -0.04 ± 0.94 | 0.07 ± 0.80 | **0.32 ± 0.45** |
| LENS RCP8.5 2006-2100 | -0.02 ± 0.45 | **1.49 ± 0.56** | 0.04 ± 0.55 | 0.05 ± 0.52 | **0.38 ± 0.29** |
| CMIP5 RCP4.5 2006-2100 | **0.16 ± 0.43** | -0.01 ± 0.66 | *0.30 ± 0.86* | 0.08 ± 0.76 | 0.13 ± 0.47 |
| CMIP5 RCP8.5 2006-2100 | **0.32 ± 0.54** | **0.56 ± 0.93** | **0.41 ± 0.75** | 0.09 ± 0.67 | **0.36 ± 0.48** |

Supplementary Table S2: Seasonal trends in the Amundsen Sea wind timeseries. PITT wind trends are shown as mean ± 1 standard deviation of the distribution of trends in ensemble members; m/s/century. Trends in italic/bold/bold underline are significantly different from zero at the 90%/95%/99% confidence level under a one-sample t-test. The seasonal trends are calculated from seasonal means while, as elsewhere in the paper, the annual trends are calculated from all monthly data after the application of a 2-year running mean.

| | Summer DJF | Autumn MAM | Winter JJA | Spring SON | Annual |
|---|---|---|---|---|---|
| PACE vs. LENS 1920-2005 | *0.09* | 0.68 | **<u>0.00</u>** | **0.01** | **<u>0.01</u>** |
| LENS RCP8.5 vs. MENS RCP4.5 2006-2080 | 0.23 | 0.22 | 0.14 | 0.13 | 0.21 |
| LENS RCP8.5 vs. MENS RCP4.5 2006-2100 | 0.37 | **0.02** | **0.04** | *0.10* | *0.05* |
| CMIP5 RCP8.5 vs. CMIP5 RCP4.5 2006-2100 | 0.10 | **<u>0.00</u>** | 0.30 | 0.48 | **0.03** |

Supplementary Table S3: Inter-ensemble differences in trends. The stated values are the p value of a two-sample t-test of the differences between ensemble trend distributions. Values in italic/bold/bold underline are sufficient to reject the null hypothesis at the 90%/95%/99% confidence level. For PACE vs. LENS, the null hypothesis is that the ensemble mean trends are equal, a two-tailed test. For the projection comparisions, the null hypothesis is that the mean RCP8.5 trend is no higher than the mean RCP4.5 trend, a one-tailed test.

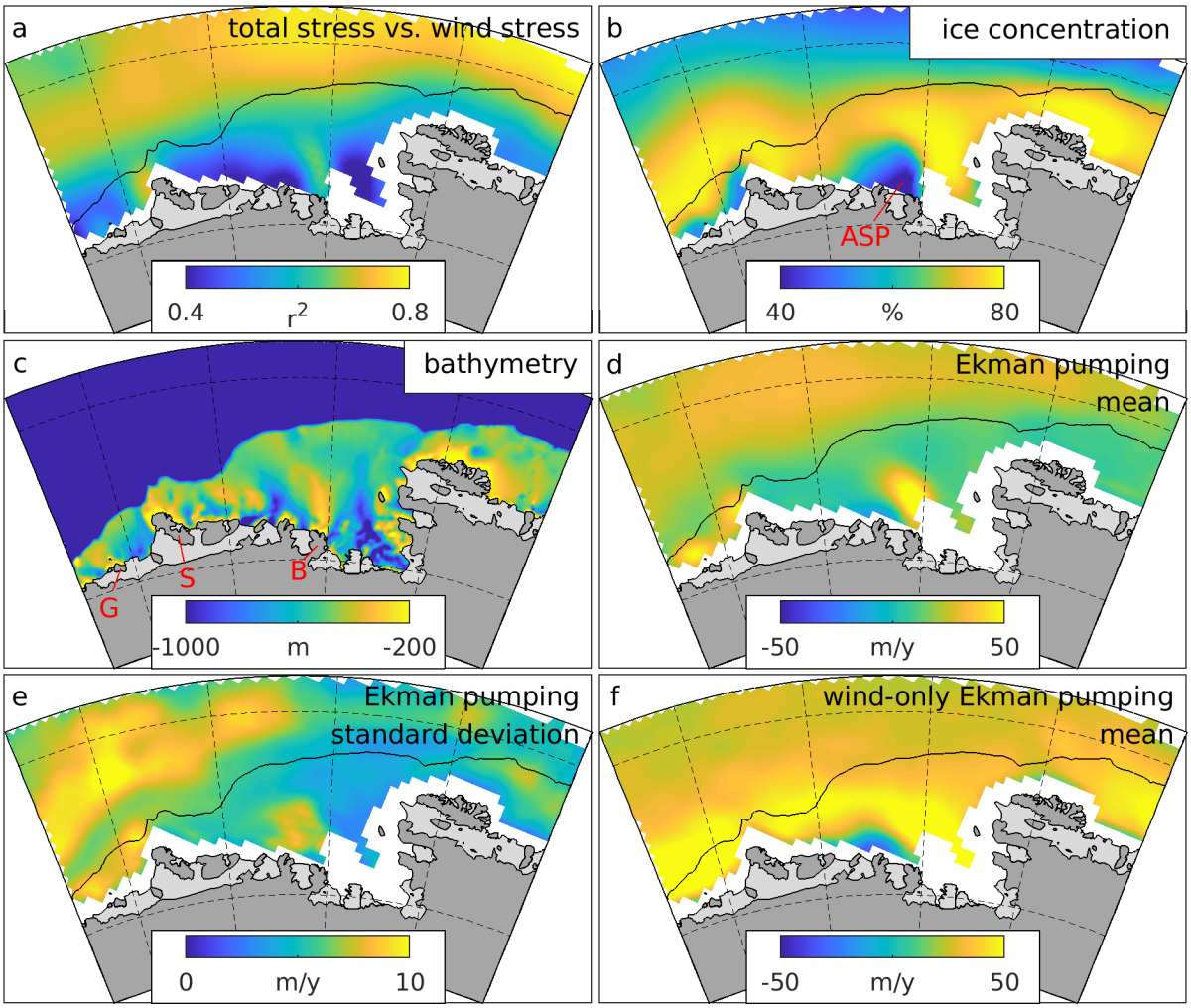


Supplementary Figure S1: Details of surface stress on the Amundsen Sea, calculated from ERA-Interim reanalysis winds and satellite-tracked sea ice drift (Methods). a) Vector correlation between total stress and wind-only stress, calculated using monthly anomalies from seasonal climatology (Methods). b) Mean sea ice concentration. c) Bathymetry. d) Mean Ekman pumping calculated from total stress. e) Standard deviation of Ekman pumping calculated from total stress (after 2-year running mean). f) Mean Ekman pumping calculated from wind-only stress. ASP: Amundsen Sea Polynya, G: Grant Island, S: Siple Island, B: Bear Island. All quantities are shown over 1992—2016.

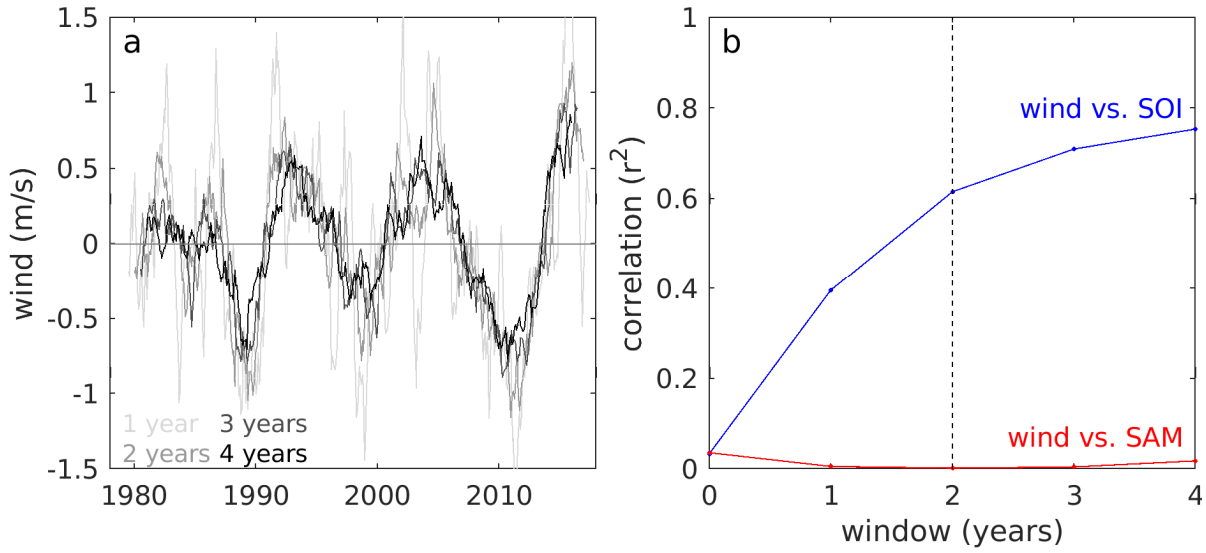


788

789 Supplementary Figure S2: Dependence of Amundsen Sea wind variability upon running-mean
790 window. a) PITT wind timeseries after smoothing with running means of different window
791 lengths. b) Correlation of PITT wind to Southern Oscillation Index (SOI) and Southern Annular
792 Mode (SAM) indices, as a function of running-mean window length. All time series are
793 detrended.

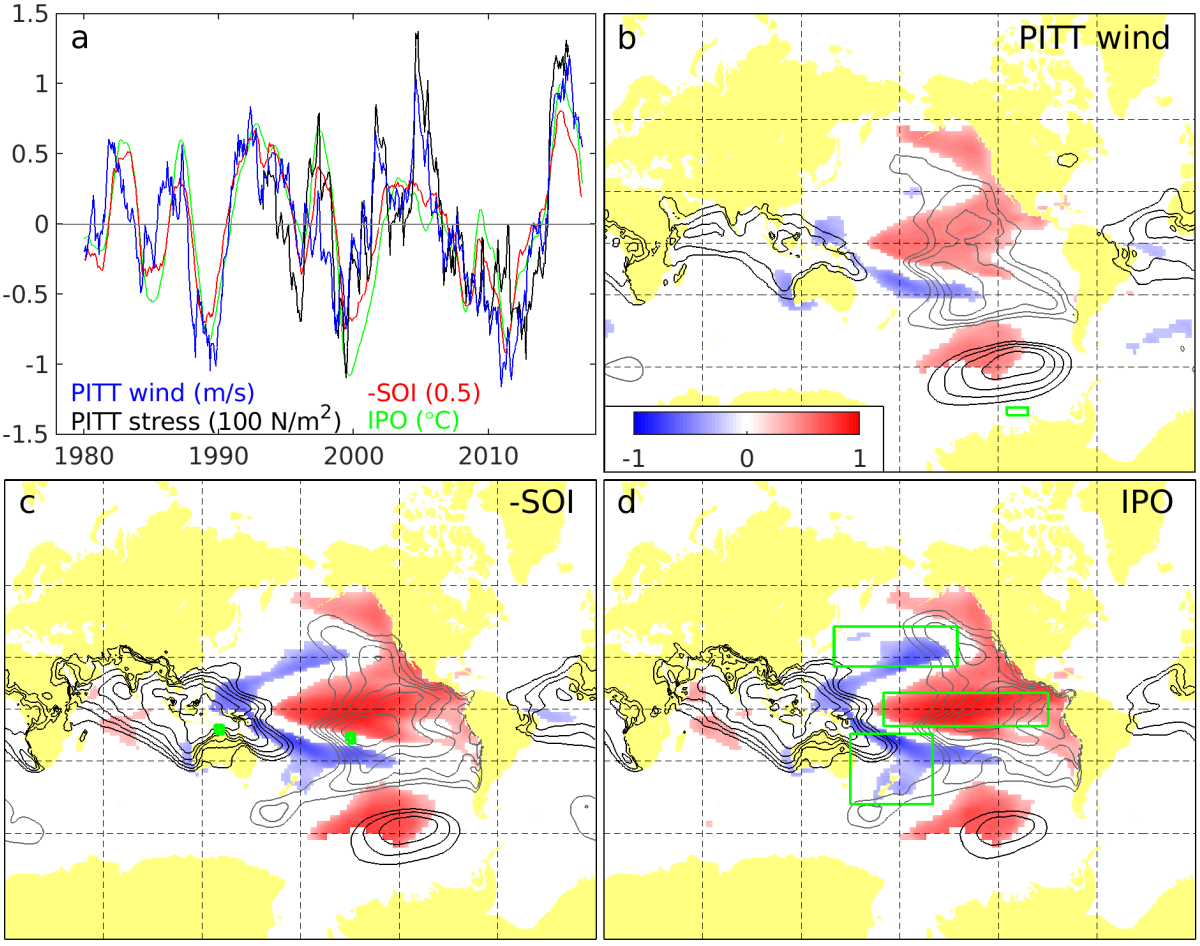


794

795 Supplementary Figure S3: As Figure 2, but with all correlations insignificant at the 95%

796 confidence level removed from panels b-d. See Methods for details of the significance testing.

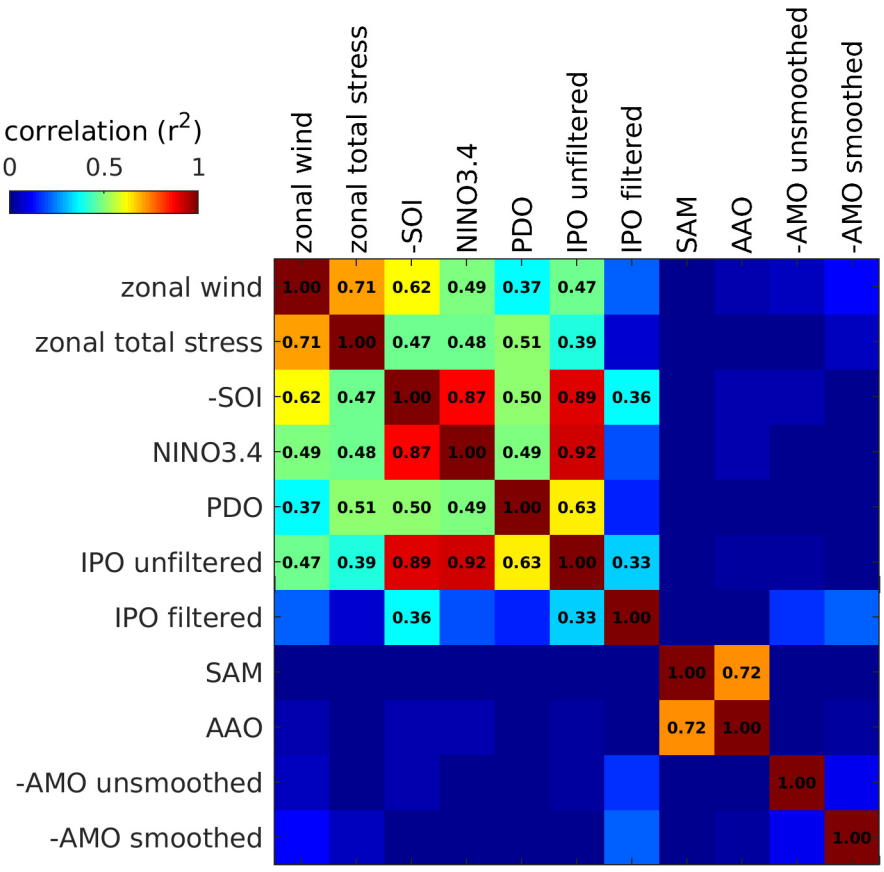


797

798 Supplementary Figure S4: Correlation between Amundsen Sea winds and climate indices
799 (Methods). Only data available during 1979—2017 are used. All timeseries have a 2-year
800 running mean applied and are detrended. The $r^2$ value is given for all correlations significant
801 at the 95% confidence level (Methods) SOI: Southern Oscillation Index; PDO: Pacific Decadal
802 Oscillation; IPO: Interdecadal Pacific Oscillation; SAM: Southern Annular Mode; AAO:
803 Antarctic Oscillation; AMO: Atlantic Multidecadal Oscillation.

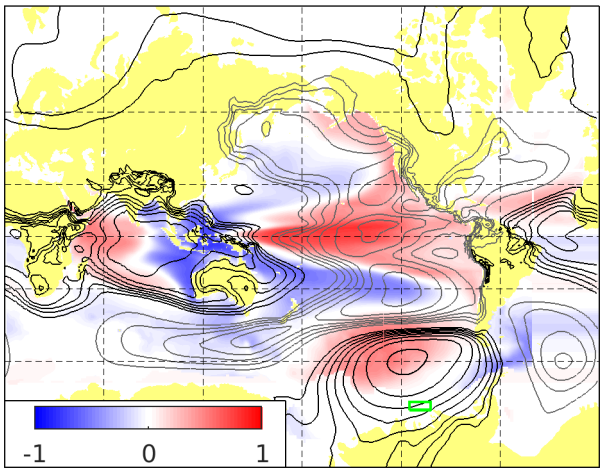


Supplementary Figure S5: Linkages between Amundsen Sea winds and global sea-surface temperature and sea-level pressure within the PACE ensemble. The plotting is identical to Supplementary Figure S3b, but for the PACE ensemble mean during 1920—2005. Relative to Supplementary Figure S3b, the longer period of data availability means that lower correlations are significant.

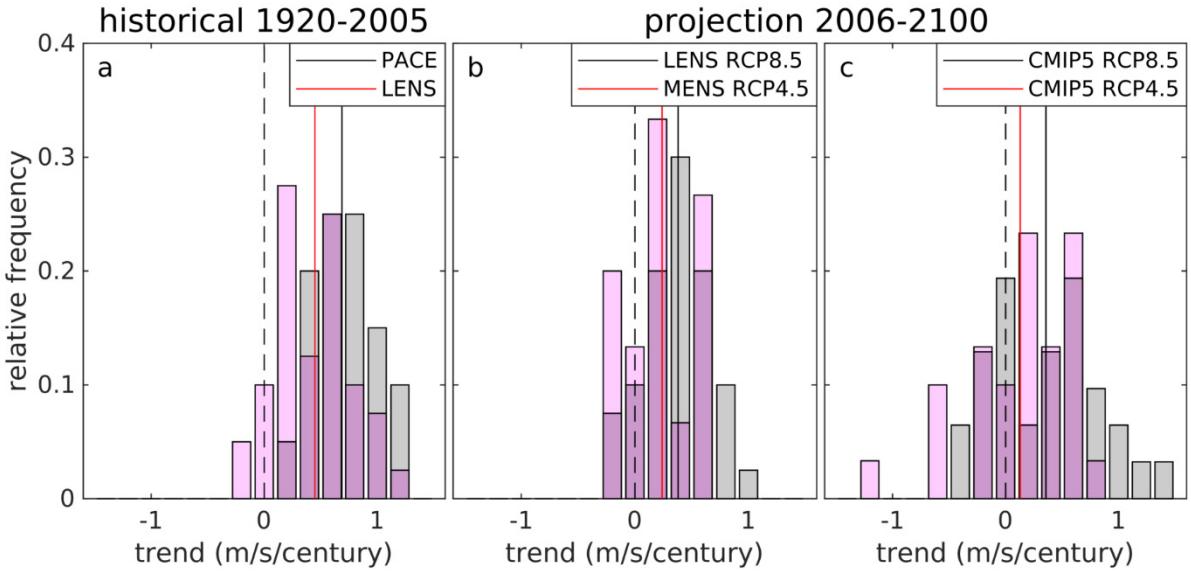


Supplementary Figure S6: Histograms of trends within the members of each ensemble. Solid vertical lines denote the ensemble means. Within each ensemble, each member's trend is equally plausible, so the spread in trends quantifies the uncertainty in the historical and projected trends. Members of the PACE, LENS, and MENS ensembles all use the same model, so their ensemble spread is caused by internal climate variability. The CMIP5 ensembles include many different models, so their larger ensemble spread is caused by both internal variability and model structural uncertainty. Note that the MENS trend is calculated over 2006-2080.

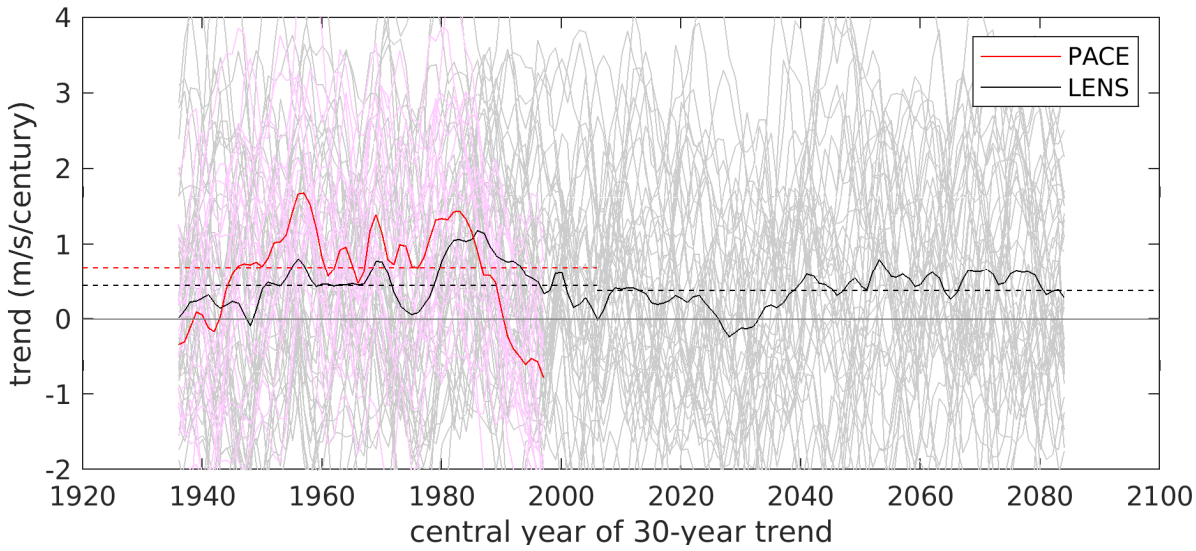


Supplementary Figure S7: Evolution of trends in Amundsen Sea winds within the PACE and LENS ensembles. Red and black solid lines show rolling 30-year sub-trends for the ensemble means from PACE and LENS, respectively. Pink and grey lines show trends for the individual ensemble members. Red and black dashed lines show the long-term (1920-2005 and 2006-2100) ensemble-mean trends (Table 1). The trend variation is not smooth as a result of decadal variability, intra-ensemble spread, and historical variability in natural radiative forcings.